Inorganic Chemistry

Article

pubs.acs.org/IC

Ligand-Based Charge-Transfer Luminescence in Ionic Cyclometalated Iridium(III) Complexes Bearing a Pyrene-Functionalized Bipyridine Ligand: A Joint Theoretical and Experimental Study

Edwin C. Constable,[†] Markus Neuburger,[†] Pirmin Rösel,[†] Gabriel E. Schneider,[†] Jennifer A. Zampese,[†] Catherine E. Housecroft,*[,†] Filippo Monti,[‡] Nicola Armaroli,*[,‡] Rubén D. Costa,[§,#] and Enrique Ortí*[,§]

[†]Department of Chemistry, University of Basel, Spitalstrasse 51, CH-4056, Basel, Switzerland

[‡]Istituto per la Sintesi Organica e la Fotoreattività, Consiglio Nazionale delle Ricerche, Via P. Gobetti 101, I-40129, Bologna, Italy

[§]Instituto de Ciencia Molecular, Universidad de Valencia, Catedrático José Beltrán 2, E-46980, Paterna, Spain

Supporting Information

ABSTRACT: Two new heteroleptic iridium(III) complexes $[Ir(ppy)_2(pyr_2bpy)][PF_6]$ ($[\mathbf{1a}][PF_6]$) and $[Ir(dfppy)_2(pyr_2bpy)][PF_6]$ ($[\mathbf{2a}][PF_6]$), where Hppy = 2-phenylpyridine, Hdfppy = 2-(3,5-difluorophenyl)pyridine, and pyr_2bpy = 5,5′-bis(pyren-1-yl)-2,2′-bipyridine, have been synthesized and fully characterized. The single-crystal structures of pyr_2bpy and the complexes $4\{[\mathbf{1a}][PF_6]\}\cdot 2CH_2Cl_2\cdot 9H_2O$ and $[\mathbf{2a}][PF_6]\cdot 0.25CH_2Cl_2\cdot H_2O$ have been determined. The effect of the pyrene substituents on the electronic properties is investigated through a comprehensive photophysical and theoretical study on the two complexes in comparison to reference complexes without substituents on the ancillary ligand ($[\mathbf{1}][PF_6]$ and $[\mathbf{2}][PF_6]$) and by making absorption and luminescence titrations of ligand pyr_2bpy. Both theory and experiment show that the intense and broad band appearing in the 400−500 nm region of the absorption spectra of $[\mathbf{1a}][PF_6]$ and $[\mathbf{2a}][PF_6]$ is due to intramolecular charge-transfer (ICT) transitions from the pyrene substituents to the bipyridine ligand. $[\mathbf{1a}][PF_6]$ and $[\mathbf{2a}][PF_6]$ exhibit luminescence bands centered above 650 nm, attributed to a charge-transfer triplet state located on the pyr_2bpy ligand, lying at lower energy than the strongly emitting Ir-ppy→bpy triplet states of the complexes lacking the pyrene fragments. Such luminescence, detected both at room temperature and 77 K, shows that the appendage of luminophoric moieties to luminescent Ir-based centers may further widen the emission tuneability of this exploited class of luminescent materials through purely electrostatic effects exerted on a properly designed N^N ancillary ligand.

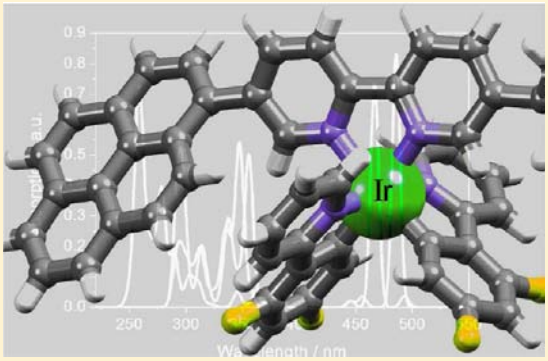

INTRODUCTION

Third-row transition-metal complexes (TMCs), particularly those containing ruthenium(II) and iridium(III) metal centers, have attracted considerable attention because of the number of remarkable features such as synthetic versatility, high photochemical and thermal stability, exceptional photophysical properties, and wide applicability in light-harvesting and electroluminescent devices.[1,2] The latter is the main field of potential application for iridium complexes, which are used as phosphorescence emitters in organic light-emitting diodes (OLEDs) and most recently in light-emitting electrochemical cells (LECs).[1b,m,3] Other applications involve a variety of technological fields such as sensing,[4] photoinduced reduction of H_2O to H_2,[5] multiphoton excitation for up-converted lasing, 3D data storage, and optical power limiting.[6] These developments have been facilitated by the simple synthetic routes leading to TMCs, which can be prepared with a wide variety of ligands that enable fine-tuning of their electronic and photophysical properties.

A recent development in ionic Ir(III) transition-metal complexes (Ir-iTMC) involves the preparation of hybrid materials incorporating organic semiconducting or light-harvesting units,[7] with the aim of combining different properties in a single material. For instance, highly efficient deep-red lighting devices have been obtained with an Ir-iTMC which incorporates a perylenediimide (PDI) that acts as an electron transporting moiety with efficient red emission.[7b] Another example is the use of Ir-iTMCs tethered to a boron-dipyrromethene (Bodipy) unit, in which an efficient energy transfer to the long-lived triplet level of the bodipy moiety demonstrated the potential applicability of these materials for

Received: September 18, 2012
Published: December 26, 2012

 © 2012 American Chemical Society dx.doi.org/10.1021/ic302026f | *Inorg. Chem.* 2013, 52, 885−897

triplet light-harvesting, a phenomenon not frequently observed.[7c]

These results suggest that there is potential for investigating Ir-iTMCs with thoroughly selected appended organic fragments characterized by particular photophysical features, such as strong absorption and/or luminescence or low-lying electronic excited states. Accordingly, we designed two new Ir-iTMCs bearing pyrene units attached to the ancillary ligand. The choice of pyrene was based on its photophysical properties that may afford valuable information upon anchoring on semiconductors and biological systems or can be exploited, more generally, in chemosensor applications.[8] Recently, Castellano and co-workers have made a neutral bis-heteroleptic iridium(III) complex with an acetylacetonate (acac) ligand functionalized with pyrene and perylene moieties.[9] In this work, they demonstrated an effective pathway for populating the triplet excited states of the aromatic moieties. However, these electronic levels are dark and do not exhibit phosphorescence at room temperature.[9]

Herein we describe the synthesis of four ionic heteroleptic iridium(III) complexes combining two different cyclometalated ligands 2-phenylpyridine (Hppy) and 2-(3,5-difluorophenyl)-pyridine (Hdfppy), with two ancillary ligands: 2,2′-bipyridine (bpy) and its functionalized version incorporating two pyrene (pyr) units in 5,5′-positions (pyr$_2$bpy), Schemes 1 and 2. More

Scheme 1. Chemical Structures of the bpy and pyr$_2$bpy Ligands. Numbering for NMR Spectroscopic Assignments for pyr$_2$bpy is also Shown

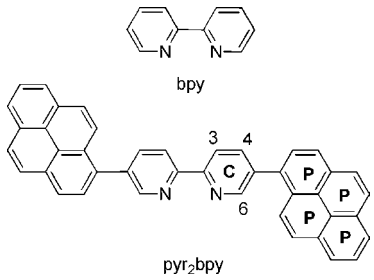

Scheme 2. Syntheses of [1][PF$_6$], [2][PF$_6$], [1a][PF$_6$], and [2a][PF$_6$]: (i) bpy or pyr$_2$bpy in MeOH/CH$_2$Cl$_2$, (ii) NH$_4$PF$_6$. Atom Labeling Used for NMR Spectroscopic Assignments; see also Scheme 1

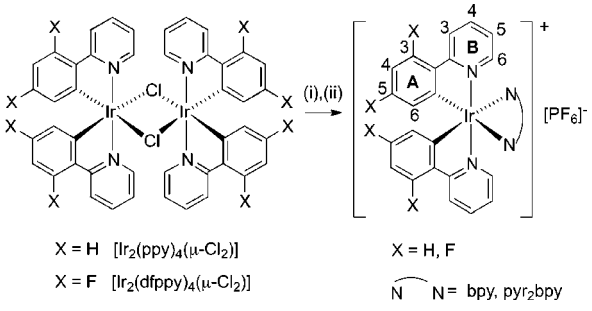

specifically, the target pyrene-based complexes are [Ir(ppy)$_2$(pyr$_2$bpy)][PF$_6$] ([**1a**][PF$_6$]) and [Ir(dfppy)$_2$(pyr$_2$bpy)][PF$_6$] ([**2a**][PF$_6$]), and the respective reference complexes [Ir(ppy)$_2$(bpy)][PF$_6$] ([**1**][PF$_6$]) and [Ir(dfppy)$_2$(bpy)][PF$_6$] ([**2**][PF$_6$]) (Scheme 2). Based on complete photophysical and theoretical studies, we conclude that, similar to the analogous neutral iridium(III) complexes of Castellano,[9] our pyrene-based Ir-iTMCs show an efficient population of the ^{3}pyr$_2$bpy state, but in contrast to neutral complexes, the phosphorescence was successfully recorded at room and low temperature conditions and exhibited a charge-transfer character, under the electrostatic influence of the nearby Ir-complexed center. This finding shows that luminescent multichromophoric Ir-complexes can be designed where the luminescence is somewhat influenced but not directly dictated by the metal complex moiety.

EXPERIMENTAL SECTION

General. Room-temperature ^{1}H and ^{13}C NMR spectra were measured on Bruker DRX500 or Bruker DRX600 spectrometers. Electrospray ionization (ESI) and EI mass spectra were recorded on a Bruker Esquire 3000 plus or VG 70−250 instrument, respectively. FT-IR spectra were recorded using a Shimadzu 8400S instrument using a Golden Gate diamond ATR accessory. An Eco Chemie Autolab PGSTAT 20 was used for the electrochemical measurements with a glassy carbon working electrode, a platinum mesh for the counter electrode, and a silver wire as the reference electrode; the solvent was dry MeCN with 0.1 M [n-Bu$_4$N][PF$_6$] as supporting electrolyte, CV scan rate was 100 mV s^{-1}, and ferrocene (Fc) was used as an external standard at the end of every experiment. A Biotage Initiator 8 reactor was used for reactions carried out under microwave conditions.

Pyren-1-ylboronic acid was purchased from Aldrich and used as received. [Ir(ppy)$_2$(μ-Cl)]$_2$ and [Ir(dfppy)$_2$(μ-Cl)]$_2$ were prepared by the literature method.[10] Compounds [**1**][PF$_6$] and [**2**][PF$_6$] were prepared as previously described.[1e,11]

5,5′-Bis(pyren-1-yl)-2,2′-bipyridine (pyr$_2$bpy). Pyren-1-ylboronic acid (1.00 g, 4.06 mmol), 5,5′-dibromo-2,2′-bipyridine[12−14] (593 mg, 1.89 mmol), and Na$_2$CO$_3$ (801 mg, 7.56 mmol) were dissolved in toluene (200 mL) and water (50 mL). The biphasic reaction mixture was degassed with N$_2$ (30 min) and then [Pd(PPh$_3$)$_4$] (219 mg, 189 mmol) was added. The reaction mixture was stirred at reflux for 3 days under rigorous exclusion of light. An insoluble solid was formed, which was collected on a glass sinter and washed with water (50 mL) and Et$_2$O (50 mL). The compound pyr$_2$bpy was isolated as a green-yellow solid (1.05 g, 1.89 mmol, 100%). ^{1}H NMR (500 MHz, CD$_2$Cl$_2$/CF$_3$CO$_2$D 1:1, data for protonated ligand, see discussion of ligand synthesis) δ/ppm: 9.43 (d, J = 1.8 Hz, 2H, H^{C6}), 9.15 (dd, J = 8.2, 2.0 Hz, 2H, H^{C4}), 8.91 (d, J = 8.3 Hz, 2H, H^{C3}), 8.46 (d, J = 7.9 Hz, 2H, H^{P}), 8.39 (m, 4H, H^{P}), 8.33 (m, 4H, H^{P}), 8.26 − 8.13 (overlapping, 8H, H^{P}). ^{13}C NMR (126 MHz, CD$_2$Cl$_2$/TFA 1:1) δ/ppm =149.5 (C^{C4}), 146.9 (C^{C6}), 145.6 (C^{C5}), 142.4 (C^{C2}), 134.8 (C^{PQ}), 132.7 (C^{PQ}), 132.0 (C^{PQ}), 131.6 (C^{P}), 131.0 (C^{P}), 129.9 (C^{PQ}), 128.6 (C^{P}), 128.3 (C^{P}), 128.25 (C^{PQ}), 128.2 (C^{P}), 128.15 (C^{P}), 127.9 (C^{C3}), 127.6 (C^{P}), 126.7 (C^{P}), 126.3 (C^{PQ}), 125.6 (C^{PQ}), 122.8 (C^{P}) (C^{PQ} = pyrene quat. C; C^{P} = pyrene CH). EI-MS: m/z 556.2 [M]$^+$ (calcd 556.2). UV−vis (CH$_2$Cl$_2$) λ_{max} (ε/ dm^3 mol^{-1} cm^{-1}) 243 (93100), 280 (55000), 357 (55500). Emission (CH$_2$Cl$_2$, λ_{exc} = 355 nm) λ_{em} = 476 nm). Anal. Calcd for C$_{42}$H$_{24}$N$_2$·1.3H$_2$O: C, 86.96; H, 4.62; N, 4.83. Found: C, 87.08; H, 4.38; N, 4.76.

[Ir(ppy)$_2$(pyr$_2$bpy)][PF$_6$] ([1a][PF$_6$]). A suspension of [Ir(ppy)$_2$(μ-Cl)]$_2$ (61.2 mg, 0.0571 mmol) and 5,5′-bis(pyren-1-yl)-2,2′-bipyridine (63.9 mg, 0.115 mmol) in MeOH (7 mL) and CH$_2$Cl$_2$ (7 mL) was heated in a microwave reactor at 110 °C (P = 14 bar) for 1 h during which time the color changed to a clear olive-green. An excess of [NH$_4$][PF$_6$] was added and the solution was stirred for 90 min. After filtration, the red-brown residue was washed with MeOH. Purification on a short silica gel column (eluent CH$_2$Cl$_2$/MeOH 100:2), followed by column chromatography using alumina and CH$_2$Cl$_2$/MeOH 100:2 yielded [**1a**][PF$_6$] as an orange powder (100 mg, 0.0832 mmol, 72.3%). ^{1}H NMR (500 MHz, DMSO-d$_6$) δ/ppm: 9.25 (d, J = 8.4 Hz, 1H, H^{C3}), 8.69 (d, J = 8.3 Hz, 1H, H^{C4}), 8.54 (d, J = 8.2 Hz, 1H, H^{B3}), 8.43 (t, J = 6.9 Hz, 2H, H^{P}), 8.40 (d, J = 7.8 Hz, 1H, H^{P}), 8.30 (d, J = 8.9 Hz, 1H, H^{P}), 8.26 (t, J = 8.8 Hz, 2H, H^{P}), 8.19 (d, J = 1.8 Hz, 2H, H^{C6+P}), 8.17 (d, J = 4.9 Hz, 1H, H^{B6}), 8.11 (t, J = 7.8 Hz, 1H, H^{B4}), 8.07 (d, J = 7.8 Hz, 1H, H^{P}), 7.98 (d, J = 7.7 Hz, 1H, H^{A3}), 7.55 (d, J =

dx.doi.org/10.1021/ic302026f | Inorg. Chem. 2013, 52, 885−897

9.2 Hz, 1H, H^{P}), 7.32 (t, J = 6.6 Hz, 1H, H^{B5}), 6.74 (t, J = 7.4 Hz, 1H, H^{A4}), 6.69 (t, J = 7.3 Hz, 1H, H^{A5}), 6.28 (d, J = 7.4 Hz, 1H, H^{A6}). ^{13}C (126 MHz, DMSO-d_6) δ /ppm 167.4 (C^{B2}), 154.4 (C^{C2}), 151.0 ($C^{B6/C6}$), 150.8 (C^{A1}), 150.2 ($C^{B6/C6}$), 144.3 (C^{A2}), 141.4 (C^{C4}), 140.3 (C^{C5}), 139.5 (C^{B4}), 131.9 (C^{PQ}), 131.6 (C^{A6}), 131.2 (C^{PQ}), 130.6 (C^{A5}), 130.5 (C^{PQ}), 129.3 (C^{P}), 129.2 (C^{P}), 128.5 (C^{P}), 127.8 (C^{P}), 127.4 (C^{P}), 126.6 (C^{P}), 126.0 (2 overlapping C^{P}), 125.9 (C^{C3}), 125.8 (C^{A3}), 124.8 (C^{B5}), 124.4 (C^{PQ}), 123.0 (C^{P}), 122.8 (C^{A4}), 120.5 (C^{B3}) (C^{PQ} = pyrene quat. C; C^{P} = pyrene CH; 3 C^{PQ} signals not resolved). IR (neat ν /cm^{-1}): 3038 (m), 2287 (w), 2037 (w), 1981 (w), 1607 (m), 1582 (m), 1475 (s), 1421 (m), 1377 (m), 1313 (m), 1267 (m), 1244 (m), 1161 (m), 1063 (m), 1030 (m), 833 (s), 756 (s), 721 (s), 692 (m), 681 (m), 631 (m). ESI-MS m/z: 1057.2 $[M - PF_6]^+$ (calcd 1057.3). Anal. Calcd for $C_{64}H_{40}F_6IrN_4P{\cdot}2.5H_2O$: C, 61.63; H, 3.64; N, 4.49. Found: C, 61.60; H, 3.46; N, 4.72. E/V (vs Cp_2Fe) +1.18 (irr), −1.36 (irr), $E_{1/2}$ −1.65 (quasi-rev).

[Ir(dfppy)$_2$(pyr$_2$bpy)][PF$_6$] ([2a][PF$_6$]). A yellow suspension of $[Ir(dfppy)_2Cl]_2$ (69.3 mg, 0.0570 mmol) and 5,5′-bis(pyren-1-yl)-2,2′-bipyridine (63.9 mg, 0.115 mmol) in MeOH (5 mL) was heated in a microwave reactor at 120 °C (P = 14 bar) for 1 h. The bright yellow color changed to green-yellow with a black precipitate. The mixture was heated for a further 30 min at 140 °C (P = 22 bar). An excess of $[NH_4][PF_6]$ was added and the mixture was stirred for 30 min. After filtration, the residue was washed with water and Et_2O. The residue was purified on a short silica gel column (CH_2Cl_2/MeOH 10:1) and [**2a**][PF_6] was isolated as a yellow-orange solid (143 mg, 0.112 mmol, 97.6%). ^{1}H NMR (500 MHz, DMSO-d_6) δ/ppm: 9.29 (d, J = 8.3 Hz, 1H, H^{C3}), 8.76 (dd, J = 8.3, 2.1 Hz, 1H, H^{C4}), 8.58 (d, J = 8.3 Hz, 1H, H^{B3}), 8.47 (d, J = 8.0 Hz, 1H, H^{P}), 8.41 (d, J = 7.7 Hz, 2H, H^{2P}), 8.32 (d, J = 9.0 Hz, 1H, H^{P}), 8.27 (d, J = 9.0 Hz, 1H, H^{P}), 8.25−8.17 (overlapping m, 5H, $H^{B6+C6+B4+2P}$), 8.13 (d, J = 7.8 Hz, 1H, H^{P}), 7.55 (d, J = 9.2 Hz, 1H, H^{P}), 7.41 (t, J = 6.6 Hz, 1H, H^{B5}), 6.71 (m, 1H, H^{A4}), 5.73 (dd, J = 8.3, 2.2 Hz, 1H, H^{A6}). ^{13}C (126 MHz, DMSO-d_6) δ /ppm 162.8 (C^{A5}), 161.9 (C^{B2}), 159.1 (C^{A3}), 153.0 (C^{C2}), 150.4 (C^{C6}),150.2 (C^{B6}), 140.8 (C^{C4}), 139.4 (C^{C5}), 139.7 (C^{B4}), 130.9 (C^{PQ}), 130.4 (C^{PQ}), 129.7 (C^{PQ}), 129.6 (C^{PQ}), 129.5 (C^{PQ}), 128.2 (C^{P}), 128.1 (C^{P}), 127.6 (C^{P}), 127.5 (C^{A2}), 126.9 (C^{P}), 126.5 (C^{P}), 125.8 (C^{P}), 125.3 (C^{C3}), 125.2 (C^{P}), 124.9 (C^{P}),124.4 (C^{B5}), 123.4 (C^{PQ}), 123.0 (C^{B3}), 121.9 (C^{P}), 113.1 (C^{PQ+A6}), 98.5 (C^{A4}), (C^{PQ} = pyrene quat. C; C^{P} = pyrene CH; signal for C^{A1} not resolved). IR (neat ν /cm^{-1}): 3056 (m), 2333 (w), 2161 (m), 1981 (m), 1595 (s), 1584 (s), 1574 (s), 1560 (m), 1474 (s), 1430 (m), 1405 (m), 1295 (m), 1271 (m), 1246 (m), 1199 (m), 1162 (m), 1120 (m), 1106 (s), 1042 (m), 991 (s), 877 (m), 846 (s), 831 (s), 818 (s), 787 (m), 759 (m), 736 (m), 721 (s), 714 (m), 681 (m), 603 (s). ESI-MS m/z: 1128.5 $[M - PF_6]^+$ (calcd 1129.3). Anal. Calcd for $C_{64}H_{36}F_{10}IrN_4P{\cdot}CH_2Cl_2$: C, 57.44; H, 2.82; N, 4.12. Found: C, 57.14; H, 3.04; N, 4.14. E/V (vs Cp_2Fe) +1.13 (irr), −1.36 (irr), $E_{1/2}$ −1.55 (quasi-rev), −1.81 (rev).

Crystallography: General. Data were collected on a Stoe IPDS or Nonius KappaCCD diffractometer. Data reduction, solution, and refinement used Stoe IPDS[15] software and SHELXL97,[16] or the programs COLLECT,[17] and then DENZO/SCALEPACK,[18] SIR92,[19] and CRYSTALS.[20] ORTEP figures were drawn with the program Ortep-3 for Windows,[21] and packing was analyzed using Mercury v. 2.4.[22,23] CCDC 871500 - 871502 contain the supplementary crystallographic data for this paper. These data can be obtained free of charge from The Cambridge Crystallographic Data Centre via www.ccdc.cam.ac.uk/data_request/cif.

pyr$_2$bpy. $C_{42}H_{24}N_2$, M = 556.67, yellow plate, monoclinic, space group $P2_1/c$, a = 7.378(3), b = 6.923(3), c = 26.070(12) Å, β = 94.21(3)°, U = 1328.1(10) Å^3, Z = 2, Dc = 1.392 Mg m^{-3}, μ(Mo−Kα) = 2.399 mm^{-1}, T = 173 K. Total 13452 reflections, 3235 unique, R_{int} = 0.149. Refinement of 200 parameters using 1624 reflections with $I > 0.9\sigma(I)$ converged at final $R1$ = 0.1048 ($R1$ all data =0.1911), $wR2$ = 0.0791 ($wR2$ all data =0.1196), gof =1.0985.

4{[1a][PF$_6$]}·2CH$_2$Cl$_2$·9H$_2$O. $C_{258}H_{182}Cl_4F_{24}Ir_4N_{16}O_9P_4$, M = 5140.80, yellow block, monoclinic, space group $P2_1/c$, a = 13.769(3), b = 35.021(7), c = 12.961(3) Å, β = 109.09(3)°, U = 5906(2) Å^3, Z = 1, D_c = 1.440 Mg m^{-3}, μ(Mo−Kα) = 2.399 mm^{-1}, T = 173 K. Total 124190 reflections, 12876 unique, R_{int} = 0.1162. Refinement of 748 parameters using 11910 reflections with $I > 2\sigma$ (I) converged at final $R1$ = 0.0436 ($R1$ all data =0.0469), $wR2$ = 0.1139 ($wR2$ all data =0.1166), gof =1.084.

[2a][PF$_6$]·0.25CH$_2$Cl$_2$·H$_2$O. $C_{64.25}H_{38.50}Cl_{0.50}F_{10}IrN_4OP$, M = 1313.39, orange block, triclinic, space group $P-1$, a = 12.7442(11), b = 15.7615(13), c = 16.2764(14) Å, α = 103.458(7), β = 110.144(6), γ = 111.389(6)°, U = 2606.9(4) Å^3, Z = 2, D_c = 1.671 Mg m^{-3}, μ(Mo−Kα) = 2.703 mm^{-1}, T = 173 K. Total 72762 reflections, 13061 unique, R_{int} = 0.0630. Refinement of 800 parameters using 12852 reflections with $I > 2\sigma$ (I) converged at final $R1$ = 0.0282 ($R1$ all data =0.0287), $wR2$ = 0.0766 ($wR2$ all data =0.0770), gof =1.100.

Photophysical Characterization. All photophysical investigations were carried out in spectroscopic grade solvents: dichloromethane, toluene, and acetonitrile. Absorption spectra were recorded with a Perkin-Elmer Lambda 950 spectrophotometer. For photoluminescence experiments, the samples were placed in fluorometric 1 cm path cuvettes and, when needed, purged from oxygen by bubbling with argon for at least 15 min. Uncorrected emission spectra were obtained with an Edinburgh FLS920 spectrometer equipped with a Peltier-cooled Hamamatsu R928 photomultiplier tube (185−850 nm). An Edinburgh Xe900 450 W xenon arc lamp was used as the excitation light source. Corrected spectra were obtained via a calibration curve supplied with the instrument. Photoluminescence quantum yields (Φ_{em} or PLQY) in solution were obtained from corrected spectra on a wavelength scale (nm) and measured according to the approach described by Demas and Crosby[24] using an air-equilibrated $[Ru(bpy)_3]Cl_2$ water solution (Φ_{em} = 2.8%)[25] as standard. Excited-state lifetimes (τ) were determined with the single-photon counting technique by means of the same Edinburgh FLS920 spectrometer using a laser diode as the excitation source (1 MHz; λ_{exc} = 407 nm; 200 ps time resolution after deconvolution) and the above-mentioned PMT as the detector. Alternatively, the lifetimes were measured with an IBH single-photon counting spectrometer equipped either with a thyratron gated nitrogen lamp (2 to 40 kHz; λ_{exc} = 337 nm; 0.5 ns time resolution), or pulsed NanoLED excitation sources (λ_{exc} at 278, 331, 465, and 560 nm; pulse width ≤0.3 ns); the detector was a red-sensitive (185−850 nm) Hamamatsu R-3237−01 PMT. Analysis of the luminescence decay profiles vs time was accomplished with the Decay Analysis Software provided by the manufacturers, and the quality of the fit was assessed by the χ^2 value close to unity with the residuals regularly distributed along the time axis. To record the 77 K luminescence spectra, the samples were put in quartz tubes (2 mm inner diameter) and inserted in a special quartz Dewar flask filled up with liquid nitrogen. 77 K phosphorescence spectra and lifetimes of the organic molecules were acquired using the same Edinburgh FLS920 spectrometer using a μF 920H flash lamp as excitation source.

Theoretical Characterization. Density functional theory (DFT) calculations were carried out with the A.01 revision of the Gaussian 09 program package.[26] All calculations were performed without symmetry considerations. As a first step, the ground-state geometry of complex $[1a]^+$ was optimized by using different functionals: the popular Becke's three-parameter B3LYP hybrid functional that includes the Lee−Yang−Parr correlation functional,[27] the combination of Becke's functional with Perdew−Wang's 1991 gradient-corrected correlation functional (B3PW91),[28] the Perdew−Wang exchange functional as modified by Adamo and Barone combined with PW91 correlation (mPW1PW91),[29] the hybrid functional using the 1998 revised form of the PBE exchange and correlation functional (PBEh1PBE),[30] and finally the hybrid functional of Truhlar and Zhao (M062X).[31] As basis set we decided to utilize the 6-31G** for C, H, F, and N atoms[32] and the "double- ζ" quality LANL2DZ basis set for Ir.[33] The best functional in terms of molecular geometry, computational time, and simulated absorption spectrum, calculated by using the time-dependent DFT (TD-DFT) approach, was shown to be the PBEh1PBE functional (see the Supporting Information for a full discussion of the results obtained with the different functionals). The PBEh1PBE functional was therefore used to optimize the geometry of the singlet ground state (S_0) and the lowest triplet excited state (T_1), as well as to perform the TD-DFT calculations for all the compounds

dx.doi.org/10.1021/ic302026f | Inorg. Chem. 2013, 52, 885−897

and only PBEh1PBE results are quoted in the text. In all calculations solvent effects were considered within the SCRF (self-consistent reaction field) theory using the polarized continuum model (PCM) approach to model the interaction with the solvent.[34] For this purpose, we selected CH_2Cl_2 as it is the most commonly used solvent in the photophysical characterization. As indicated in the main text, other solvents such as acetonitrile and toluene were also used for the studies carried out on the pyr_2bpy compound.

RESULTS AND DISCUSSION

Synthesis and Characterization of pyr_2bpy. The compound pyr_2bpy was synthesized by a Suzuki coupling of 5,5′-dibromo-2,2′-bipyridine with pyren-1-ylboronic acid in biphasic conditions in the presence of $[Pd(PPh_3)_4]$ with exclusion of light. The electron impact mass spectrum of the product exhibited a peak at m/z 556.2 assigned to $[M]^+$ for pyr_2bpy. The compound is poorly soluble in CH_2Cl_2, and insoluble in most other common solvents including DMSO. Protonation using TFA yields a salt that is very soluble in, for example, CH_2Cl_2 and, for this reason, solution characterization was of the protonated ligand. NMR spectra were recorded in a mixture of CF_3CO_2D and CD_2Cl_2. The ^1H and ^{13}C NMR spectra were assigned using COSY, HMQC, HMBC, and DEPT methods and were consistent with a symmetrical bpy domain, and confirmed the presence of two pyren-1-yl substituents. Single crystals of pyr_2bpy were grown by layering ethyl acetate on a CH_2Cl_2 solution of the ligand; sufficient TFA was added to the CH_2Cl_2 to solubilize the compound. Despite the presence of acid, crystals of the neutral compound were obtained and the centrosymmetric structure is presented in Figure 1. The *trans*-conformation of the bpy unit is consistent

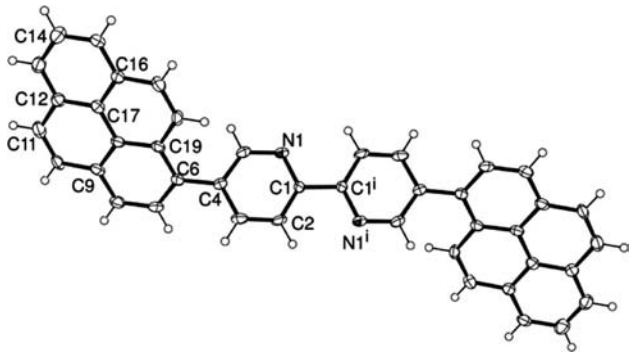

Figure 1. ORTEP diagram of the structure of the compound pyr_2bpy (ellipsoids plotted at 40% probability level). Symmetry code i = $1-x$, $1-y$, $1-z$. Selected bond distances: C1−C1^i = 1.487(7), C4−C6 = 1.472(5), C1−N1 = 1.351(4), C1−C2 = 1.380(5) Å.

with crystallization of the nonprotonated ligand. The pyrene unit is twisted 45.8° out of the plane of the bpy domain. The packing of molecules in the lattice is dominated by CH···π contacts[35] rather than by the π-stacking found in the solid-state structure of pyrene.[36]

Synthesis and Characterization of [1a][PF_6] and [2a][PF_6]. The complexes [**1a**][PF_6] and [**2a**][PF_6] were prepared by reaction of the dimer $[Ir(ppy)_2(\mu\text{-Cl})]_2$ or $[Ir(dfppy)_2(\mu\text{-Cl})]_2$ with pyr_2bpy followed by anion exchange with addition of $[NH_4][PF_6]$ (Scheme 2). The electrospray mass spectrum of each complex showed a peak envelope arising from the ion $[M - PF_6]^+$ and the isotope distribution was consistent with that calculated. The solution ^1H and ^{13}C NMR spectra were assigned by a combination of COSY, HMQC, HMBC and DEPT methods. On going from [**1a**][PF_6] to [**2a**][PF_6], the DMSO solution NMR spectrum shows the expected disappearance of signals for H^{A3} and H^{A5} (Scheme 2), and a shift in the signal for H^{A6} from δ 6.28 to 5.73 ppm. Changes in the ^{13}C NMR spectrum are consistent with the introduction of the two fluoro-substituents in ring A (Scheme 2).

X-ray quality crystals of 4{[**1a**][PF_6]}·2CH_2Cl_2·9H_2O were grown over 3 days by layering a CH_2Cl_2 solution of [**1a**][PF_6] with Et_2O, and the same method was used to obtain suitable crystals of [**2a**][PF_6]·0.25CH_2Cl_2·H_2O. Figures 2 and 3 depict

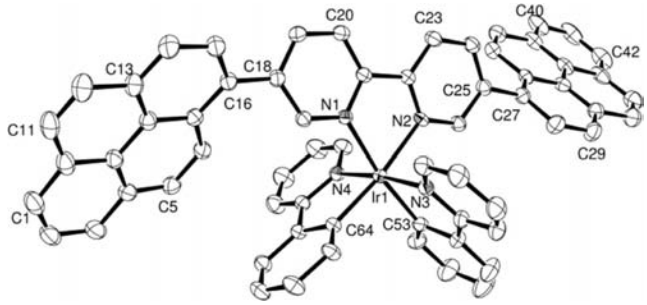

Figure 2. Structure of the $[1a]^+$ cation in 4{[**1a**]-[PF_6]}·2CH_2Cl_2·9H_2O (H atoms omitted, ellipsoids plotted at 30% probability level). Selected bond parameters: Ir1−C64 = 2.014(4), Ir1−C53 = 2.026(4), Ir1−N3 = 2.046(3), Ir1−N4 = 2.053(3), Ir1−N2 = 2.131(3), Ir1−N1 = 2.135(3) Å; N2−Ir1−N1 = 76.85(13), C53−Ir1−N3 = 80.67(17), C64−Ir1−N4 = 80.46(15), N3−Ir1−N4 = 173.05(13), C53−Ir1−N1 = 171.82(14), C64−Ir1−N2 = 172.80(14)°.

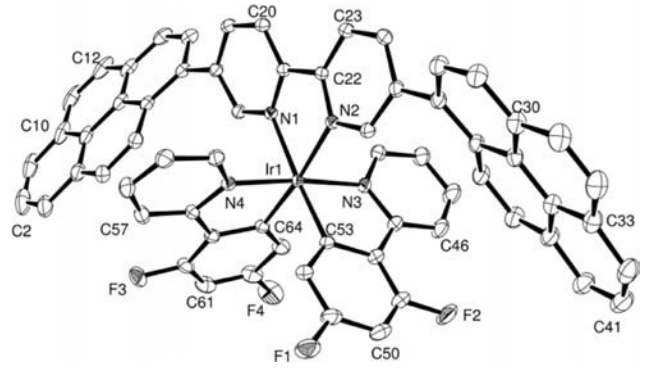

Figure 3. Structure of the $[2a]^+$ cation in [**2a**][PF_6]·0.25CH_2Cl_2·H_2O (H atoms omitted, ellipsoids plotted at 30% probability level). Selected bond parameters: Ir1−C53 = 1.998(3), Ir1−C64 = 2.001(3), Ir1−N4 = 2.034(2), Ir1−N3 = 2.039(2), Ir1−N2 = 2.125(2), Ir1−N1 = 2.134(2) Å; N2−Ir1−N1 = 76.84(9), C53−Ir1−N3 = 80.28(11), C64−Ir1−N4 = 80.49(11), N4−Ir1−N3 = 174.08(9), C53−Ir1−N1 = 175.00(9), C64−Ir1−N2 = 173.44(9)°.

the structures of the $[1a]^+$ and $[2a]^+$ cations, respectively. The octahedral geometry of the iridium(III) ion in each complex cation is, as expected, as is the *trans*-arrangement of the *N*-donors of the two cyclometalated ppy^- ligands; a search of the CSD, Conquest version 5.33 with February 2012 updates for {$Ir(ppy)_2(N^\wedge N)$} coordination spheres shows all known structures to have this arrangement.[22] The metal-bound bpy unit deviates slightly from planarity in each cation (7.8° in $[1a]^+$ and 11.6° in $[2a]^+$) and each pyrene substituent is twisted with respect to the pyridine ring to which it is attached (59.6 and 37.2° in $[1a]^+$ and 42.7 and 43.3° in $[2a]^+$). The twisting of

dx.doi.org/10.1021/ic302026f | Inorg. Chem. 2013, 52, 885−897

the pyrene units is therefore similar to that observed for the free ligand (45.8°). Only one of the pyrene substituents of $[\mathbf{1a}]^+$ is involved in face-to-face intercation π-stacking. The pyrene unit containing atom C16 stacks over that containing $C16^i$ (symmetry code i = $3-x$, $2-y$, $1-z$) in an adjacent cation; the pyrene domains are slipped with respect to one another giving an efficient interaction with an interplane separation of 3.52 Å. Similarly, in $[\mathbf{2a}][PF_6]\cdot 0.25CH_2Cl_2\cdot H_2O$, only one of the pyrene units in $[\mathbf{2a}]^+$ participates in face-to-face π-stacking. The substituent containing C27 is efficiently stacked over that containing $C27^i$ (symmetry code i = $-x$, $1-y$, $1-z$) at an interplane separation of 3.57 Å. Additional packing interactions in both compounds involve CH···π and CH···F contacts. Fractional occupancy CH_2Cl_2 and H_2O solvent molecules have been modeled in both structures.

Photophysical Properties of pyr_2bpy. The behavior of ligand pyr_2bpy was investigated and compared with that of its individual moieties (i.e., pyrene and 2,2′-bipyridine). Room-temperature (RT) absorption spectra of pyr_2bpy, pyr, and bpy in CH_2Cl_2 solution are reported in Figure 4. The absorption

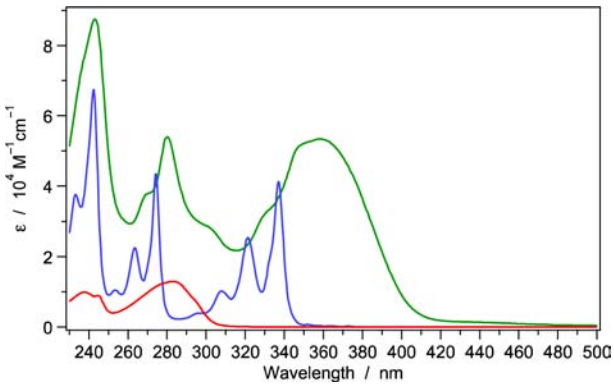

Figure 4. Absorption spectra of pyrene (pyr, blue), 2,2′-bipyridine (bpy, red) and pyr_2bpy (green) in acid-free CH_2Cl_2.

profile of pyr_2bpy in the region between 230 and 350 nm resembles that of free pyrene, though with broader and slightly red-shifted bands. At longer wavelengths, a new band centered at 360 nm is detected; this feature is absent both in pyr and bpy, and is attributed to a charge-transfer (CT) transition from the pyrene moieties to the central bipyridine unit. This is a common feature for pyrene-bipyridine dyads[37] and, in the case of pyr_2bpy, the CT nature of this state is corroborated by a remarkable red-shift upon increasing the solvent polarity. Further confirmation of the CT assignment is provided in the theoretical description of the pyr_2bpy ligand (see next section).

The absorption spectrum of pyr_2bpy (5 μM) was also recorded upon addition of increasing amounts of trifluoroacetic acid (up to 100 equivalents, Figure 5, top). In this range, three isosbestic points are found (306, 340, and 394 nm) attesting to the occurrence of one single reaction (i.e., the first protonation of the ligand at the bpy site). Notably, the absorption spectra of acid solutions of pyr_2bpy are characterized by the lack of the intense band attributed to a CT pyr→bpy transition (λ_{max} = 360 nm) and by the presence of a broader and less intense shoulder centered around 440 nm, tentatively attributed to a CT pyr→$bpyH^+$ transition. This attribution is validated by the theoretical description of the neutral and protonated pyr_2bpy species (see next section). When more than 100 equiv. of acid are added (Figure 5, bottom), the new CT band is further red-

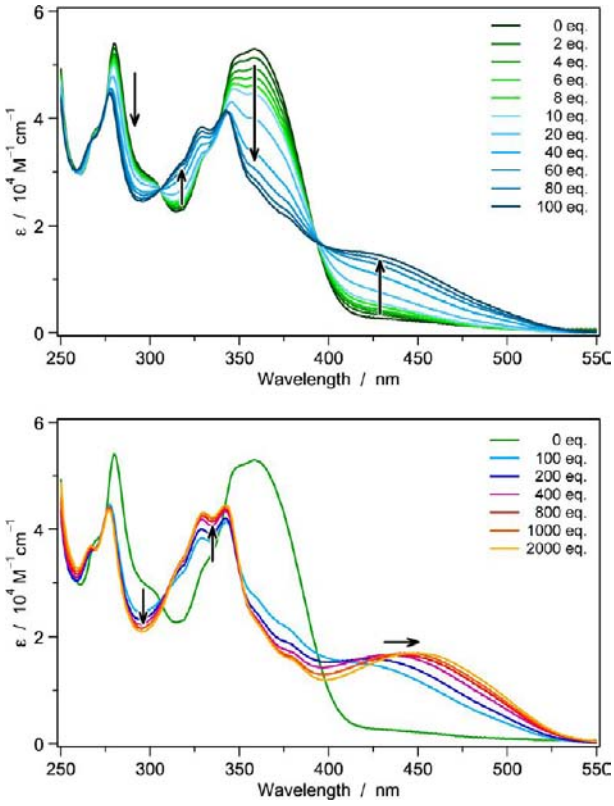

Figure 5. Absorption spectral changes of pyr_2bpy upon addition of increasing amounts of trifluoroacetic acid in room-temperature CH_2Cl_2: (top) range between 0 and 100 equivalents of acid, three isosbestic points can be found at 306, 340, and 394 nm; (bottom) general overview up to the addition of 2000 equivalents, the further shift of the CT band toward longer wavelengths can be observed.

shifted and clean isosbestic points are no longer observable, probably due to the strong perturbation of the intrinsic physical properties of the solvent (e.g., ionic strength, dielectric constant, and refractive index) induced by the presence of high amounts of trifluoroacetic acid. In principle, a second protonation of the ligand is possible, but we can assume that, under these experimental conditions, the diprotonated form $[(pyr_2bpy)H_2]^{2+}$ is quantitatively dissociated into $[(pyr_2bpy)H]^+ + H^+$ because of the acid strength of 2,2′-bypridinium dications, so that it can be neglected.[38]

The pyr_2bpy free-ligand exhibits a strong fluorescence at room temperature ($\Phi \approx 60\%$, see Figure 6 and Table 1 for details). The emission profile is unstructured and relatively broad, hence significantly different to pristine pyrene. While the emission energy of pyr is almost solvent-independent, the band of pyr_2bpy undergoes a considerable solvent-dependent Stokes shift (Table 1); its maximum lies at 448 nm in CH_2Cl_2, but is shifted to higher energies as the solvent polarity is decreased (e.g., 425 nm in toluene). Such behavior, which is well-known for electron donor−acceptor systems, further suggests the presence of a fluorescent intramolecular charge-transfer (ICT) state in both polar and nonpolar solvents.[37] Importantly, although this ICT state is strongly destabilized in nonpolar solvents, it remains lower-lying than the first singlet excited state of pyr (Figure 6); therefore, no pyrene-based emission is detected in any case for pyr_2bpy. At low temperature, fluorescence bands become more structured and vibrationally

dx.doi.org/10.1021/ic302026f | Inorg. Chem. 2013, 52, 885−897

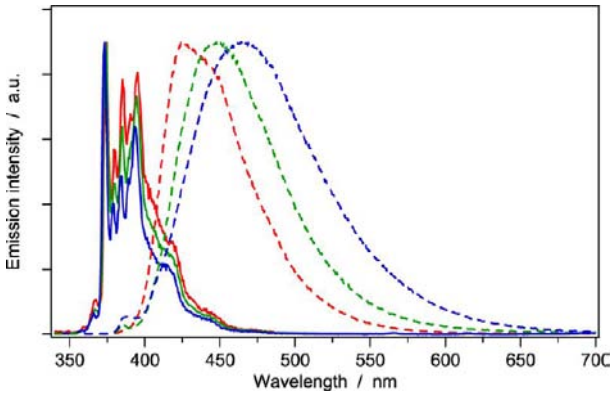

Figure 6. Normalized emission spectra of pyr (solid) and pyr_2bpy (dashed) at room temperature in different solvents: toluene (red), dichloromethane (green), and acetonitrile (blue); λ_{exc} = 310 nm.

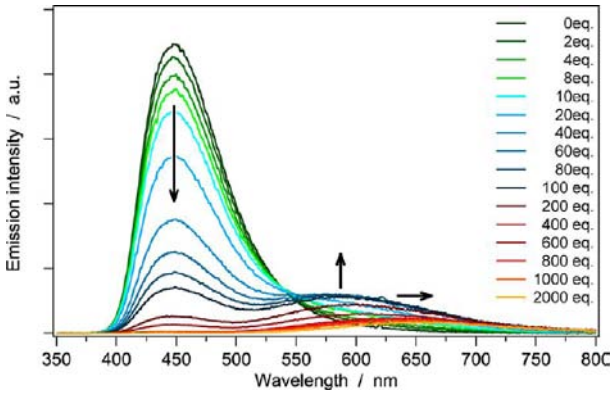

Figure 7. Emission spectral changes of pyr_2bpy upon addition of increasing amounts of trifluoroacetic acid in CH_2Cl_2 at room temperature. λ_{exc} = 306 nm, corresponding to an isosbestic point (see Figure 5, top).

resolved (both in the case of pyr and pyr_2bpy), but virtually no energy shift is observed when decreasing the temperature.

To investigate the emission properties of pyr_2bpy in the presence of a cationic species at the bpy site, emission spectra were recorded in CH_2Cl_2 during the titration with trifluoroacetic acid (Figure 7). The strong fluorescence band of the free ligand is promptly quenched upon addition of few equivalents of acid, and a weaker emission is found at around 650 nm (Φ = 5.0%, τ = 500 ps in CH_2Cl_2). The lower energy of this new emitting state further corroborates its ICT nature (pyr→$bpyH^+$) because intramolecular charge transfer is clearly favored in the presence of a protonated acceptor. It should be noted that upon addition of more than 100 equivalents of acid, the energy of this ICT state is further decreased, likely due to a dramatically enhanced polarity of the solvent environment.

Because iridium(III) complexes are triplet emitters due to the high spin−orbit coupling of the central metal ion, we recorded luminescence spectra of the pyr_2bpy free ligand at low temperature in order to evaluate the energy of the triplet excited state. The phosphorescence spectra, recorded at 77 K, are virtually solvent independent and show that, while the pyrene triplet emission is found at 590 nm (with a lifetime of ~0.5 s), the pyr_2bpy phosphorescence appears at 626 nm, with a substantially shorter lifetime (~10 ms, Figure 8). No triplet emission from the protonated ligand could be detected.

Theoretical Description of the Ground and Excited States of pyr_2bpy. To gain insight into the molecular and electronic structures and the optical properties of both neutral and protonated pyr_2bpy species, theoretical calculations were performed in the framework of the DFT and TD-DFT

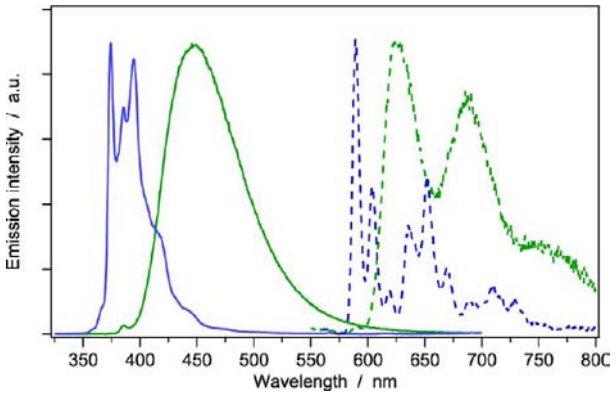

Figure 8. Fluorescence (solid lines) and phosphorescence (dashed lines) spectra of pyr (blue) and pyr_2bpy (green) in acid-free CH_2Cl_2 (λ_{exc} = 280 nm). Phosphorescence spectra were recorded at 77 K applying a delay of 50 μs to avoid residual fluorescence signal.

approaches using the PBEh1PBE functional (see the Experimental Section for full computational details). For the neutral species, the most stable structure corresponds to an *s*-trans disposition of the bpy domain in agreement with the X-ray structure shown in Figure 1. In contrast, for the protonated species, the *s-cis*-configuration is predicted to be the most stable conformer (5.2 kcal/mol lower in energy than the *s-trans*-conformer) due to the stabilization effect of the hydrogen bond formed by the N^+−H group and the vicinal N atom. The predicted molecular structure for both neutral and protonated species is very similar in terms of bond lengths, and is in good

Table 1. Photophysical Properties of pyr and pyr_2bpy in Solution. Data in Oxygen-Free and Air-Equilibrated Solutions (in Parentheses) are Given

	λ_{emi} (nm)	Φ (%)	τ (ns)	k_r (10^6 s^{-1})	k_{nr} (10^6 s^{-1})
			pyr		
toluene	373	74.0 (3.4)	310 (16.9)	2.39 (2.02)	0.84 (57.1)
CH_2Cl_2	374	30.4 (6.8)	164 (30.4)	1.85 (2.24)	4.24 (30.7)
MeCN	374	61.9 (3.7)	318 (14.3)	1.95 (2.61)	1.20 (67.3)
	λ_{emi} (nm)	Φ (%)	τ (ns)	k_r (10^8 s^{-1})	k_{nr} (10^8 s^{-1})
			pyr_2bpy		
toluene	425	87.5 (70.4)	1.4 (1.0)	6.25 (5.87)	0.90 (2.46)
CH_2Cl_2	448	61.7 (63.3)	1.7 (1.4)	3.63 (3.96)	2.26 (2.29)
MeCN	465	42.3 (33.0)	2.4 (2.0)	1.76 (1.65)	2.40 (3.35)

dx.doi.org/10.1021/ic302026f | *Inorg. Chem.* 2013, 52, 885−897

agreement with the X-ray structure. The twisting angle between the pyr and bpy units of ~53° for both neutral and protonated species is slightly overestimated compared to the X-ray diffraction value (45.8°) which will be affected by packing effects in the crystal.

Figure 9 displays the electronic density distribution calculated for the highest-occupied and lowest-unoccupied molecular orbitals (HOMO and LUMO, respectively) of neutral and protonated pyr_2bpy in their respective singlet ground states. To make the comparison with the protonated species easier, the energies and topologies shown in Figure 9 for the molecular orbitals of neutral pyr_2bpy are those obtained for the *s-cis* conformer. Almost identical energies and topologies are computed for *s-trans*-pyr_2bpy. For the neutral molecule, the molecular orbitals turn out to be distributed throughout the whole molecule, whereas protonation markedly localizes the electronic density of the HOMO and LUMO on the pyr and bpy units, respectively. Protonation also produces a stabilization of the molecular orbitals and leads to a significant reduction of the HOMO−LUMO energy gap in line with the red-shift observed in the absorption spectra.

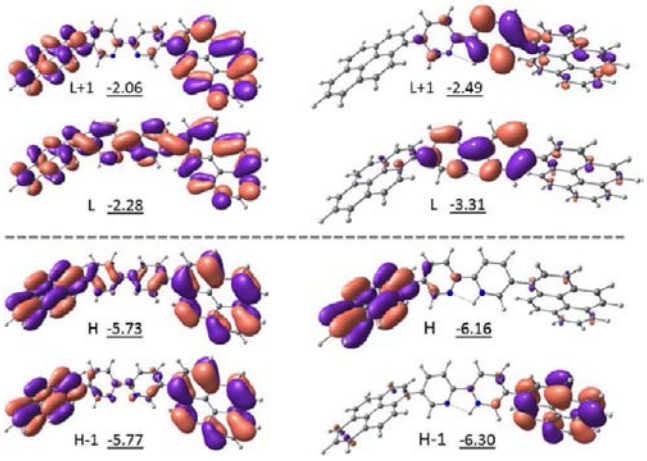

Figure 9. Electronic density contours (0.03 e $bohr^{-3}$) calculated for the HOMO, HOMO−1, LUMO, and LUMO+1 (H and L denote HOMO and LUMO, respectively) of neutral (left) and protonated (right) pyr_2bpy. Orbital energies are provided in eV.

Table 2 summarizes the vertical excitation energies and electronic nature calculated for the lowest-energy singlet excited states of neutral and protonated pyr_2bpy. As discussed in the photophysical section, the neutral species shows a broad band at 350−375 nm (Figure 4), which is ascribed to an intramolecular pyr→bpy charge transfer transition. TD-DFT calculations predict that the optical absorption between 350 and 390 nm mainly arises from the electronic transition to the S_1 and S_2 excited singlets (Table 2). These states result from the HOMO→LUMO and HOMO−1→LUMO excitations, respectively, and imply an electronic density charge transfer from the lateral pyr units to the central bpy moiety (Figure 9). The HOMO→LUMO excitation is significantly more intense (f = 1.19) than the HOMO−1→LUMO (f = 0.24) and it is calculated to slightly red-shift when increasing the polarity of the solvent (toluene: 383 nm, acetonitrile 386 nm, Table 2) in agreement with experimental trends. Calculations therefore corroborate the ICT nature of the lowest-energy band observed in the absorption spectrum. The shoulder observed in the experimental spectrum around 330 nm (Figure 4) is assigned to the less intense S_3 (f = 0.15) and S_4 (f = 0.16) states that

Table 2. TD-DFT Singlet Excited States Calculated for Neutral and Protonated pyr_2bpy in Different Solvents. Vertical Excitation Wavelengths (λ), Oscillator Strengths (f), Dominant Monoexcitations (with their Contribution in Parentheses), and Nature of the Electronic Transition are Provided

solvent	state	λ (nm)	f	dominant monoexcitation	nature
			pyr2bpy		
toluene					
	S_1	383	1.21	H → L (0.67)	pyr/bpy→bpy/pyr
	S_2	367	0.29	H−1 → L (0.67)	pyr/bpy→bpy/pyr
	S_3	345	0.13	H → L+1 (0.66)	pyr→pyr
	S_4	338	0.14	H−1 → L+1 (0.65)	pyr→pyr
CH_2Cl_2					
	S_1	385	1.19	H → L (0.67)	pyr/bpy→bpy/pyr
	S_2	367	0.24	H−1 → L (0.67)	pyr/bpy→bpy/pyr
	S_3	345	0.15	H → L+1 (0.66)	pyr→pyr
	S_4	338	0.16	H−1 → L+1 (0.65)	pyr→pyr
MeCN					
	S_1	386	1.16	H → L (0.67)	pyr/bpy→bpy/pyr
	S_2	369	0.21	H−1 → L (0.67)	pyr/bpy→bpy/pyr
	S_3	345	0.15	H → L+1 (0.66)	pyr→pyr
	S_4	337	0.17	H−1 → L+1 (0.65)	pyr→pyr
			pyr_2bpyH^+		
CH_2Cl_2					
	S_1	531	0.59	H → L (0.66)	pyr→$bpyH^+$
	S_2	504	0.05	H−-1 → L (0.66)	pyr→$bpyH^+$
	S_3	396	0.25	H−1 → L+1 (0.58) H → L+1 (0.36)	pyr→$bpyH^+$
	S_5	376	0.21	H−2 → L (0.69)	pyr→$bpyH^+$
	S_7	349	0.27	H → L+2 (0.65)	pyr→pyr
	S_8	339	0.47	H−1 → L+2 (0.65)	pyr→pyr

dx.doi.org/10.1021/ic302026f | *Inorg. Chem.* 2013, 52, 885−897

correspond to the HOMO→LUMO+1 and HOMO−1→LUMO+1 transitions, respectively, and mainly imply pyr→pyr excitations (see Table 2 and Figure 9).

Additional significant data came from the TD-DFT analysis of the protonated species. The experimental data showed the appearance of a broad band centered at 440 nm that was tentatively attributed to an ICT pyr→bpyH$^+$ transition. This assignment is corroborated by TD-DFT calculations that predict a manifold of three excited states (S_1 to S_3) lying in the 400−530 nm range, implying a charge transfer from the pyr units to the bpyH$^+$ moiety (Table 2 and Figure 9). In addition, the pyr→pyr excitations appear in the 340−350 nm range as for neutral pyr$_2$bpy and in agreement with the experimental spectrum (Figure 5).

The lowest triplet state (T_1) of both neutral and protonated pyr$_2$bpy was optimized in dichloromethane by means of the spin-unrestricted UDFT approach. Figure 10 displays the spin

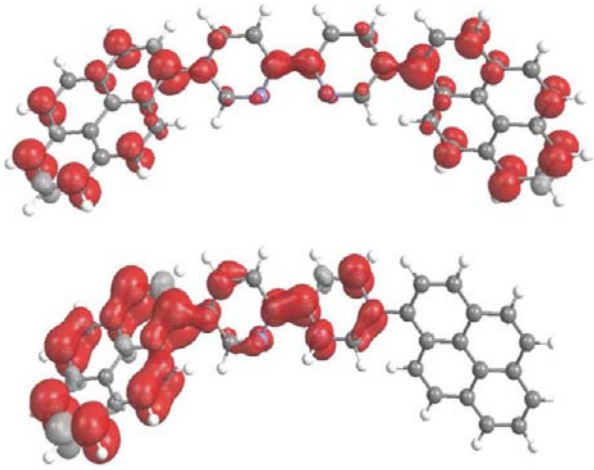

Figure 10. Spin density distribution (0.005 e bohr^{-3}) of the T_1 state for neutral (top) and protonated (bottom) pyr$_2$bpy.

density distribution calculated for T_1 for both species. It perfectly matches the topology of the HOMO→LUMO excitation (Figure 9), in which T_1 originates, and confirms the ICT nature of this state. The T_1 state is computed 1.98 eV (626 nm) above the S_0 state (adiabatic energy difference) for pyr$_2$bpy in perfect agreement with the first emission peak observed in the phosphorescence spectrum (Figure 8). For protonated pyr$_2$bpy, the T_1 state is calculated at slightly lower energies (1.78 eV above S_0), but no phosphorescence is detected experimentally for this species and no comparison can be made.

Photophysical Properties of Iridium(III) Complexes Based on the pyr$_2$bpy Ligand. Once a comprehensive picture of the photophysical behavior of pyr$_2$bpy had been obtained, the spectroscopic properties of the iridium(III) pyr$_2$bpy-based complexes [Ir(ppy)$_2$(pyr$_2$bpy)][PF$_6$] ([**1a**][PF$_6$]) and [Ir(dfppy)$_2$(pyr$_2$bpy)][PF$_6$] ([**2a**][PF$_6$]) were investigated. All the characterizations were carried out only in CH_2Cl_2 because the complexes are insoluble in nonpolar solvents (e.g., toluene) due to their ionic character, and are unstable in more coordinating solvents (e.g., acetonitrile) because the pyr$_2$bpy ligand is displaced by solvent-assisted nucleophilic attack. In fact, fluorescence spectroscopic data were consistent with increasing amounts of free ligand in MeCN solution of the complexes.

Figure 11 shows the electronic absorption spectra of complexes [**1a**][PF$_6$] and [**2a**][PF$_6$] together with those of

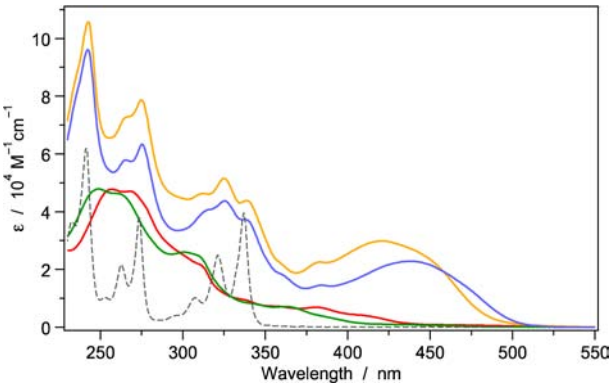

Figure 11. Absorption spectra of reference complexes [**1**][PF$_6$] (red) and [**2**][PF$_6$] (green), together with those of the target complexes [**1a**][PF$_6$] (orange) and [**2a**][PF$_6$] (blue). The pyrene spectrum is also reported (gray dashed line). All spectra are recorded in CH_2Cl_2.

the reference complexes [Ir(ppy)$_2$(bpy)][PF$_6$] ([**1**][PF$_6$]) and [Ir(dfppy)$_2$(bpy)][PF$_6$] ([**2**][PF$_6$]). In the region 230−350 nm, the absorption profiles of [**1a**][PF$_6$] and [**2a**][PF$_6$] are virtually the sum of the spectra of the pyrene moiety and the respective reference complexes. Notably, at λ > 375 nm, a broad band is observed for both pyr$_2$bpy-based complexes, reminiscent of the ICT band of the protonated pyr$_2$bpy ligand. Such a feature might be rationalized considering that, in these complexes, the pyr$_2$bpy ligand is chelating a monocationic unit (i.e., an iridium(III) center surrounded by two anionic cyclometalating ligands); in other words, the [(C^N)$_2$Ir]$^+$ moiety seems to act simply as a positive charge similar to a proton. The broad CT band is more red-shifted in the case of [**2a**][PF$_6$], which is in contrast to what is typically found for cationic iridium(III) complexes with fluoro-substituted phenylpyridine cyclometalated ligands, and which usually display blue-shifted transitions compared with unsubstituted analogues, due to HOMO stabilization[3a,39] However, in the present case, if we assume that the [(C^N)$_2$Ir]$^+$ moiety has essentially an electrostatic effect on the pyr$_2$bpy ligand, this unit experiences a more positively charged environment in the case of the fluoro-substituted complex [**2a**][PF$_6$], due to the electron-withdrawing effect of the fluoro-substituents. Accordingly, the energy of the pyr→bpy[(dfppy)$_2$Ir]$^+$ CT transition is lowered with respect to [**1a**][PF$_6$]. This electrostatic hypothesis is supported by the theoretical description performed for both pyr$_2$bpy-based complexes (see next section).

Photoluminescence studies under different conditions were performed to further elucidate the effect of the pyrene moieties on the iridium(III) complexes. While [**1**][PF$_6$] and [**2**][PF$_6$] are well-known good emitters from the lowest lying metal-to-ligand charge transfer (MLCT) state,[3a,40] [**1a**][PF$_6$] and [**2a**][PF$_6$] display very weak (Φ < 1%, τ = 4−7 ns) and unstructured emissions around 660 nm (Table 3 and Figure 12). These bands are somewhat similar to the fluorescence band of the protonated ligand (Figure 7), but are more structured, red-shifted, and longer-lived (∼5 ns vs ∼0.5 ns). Moreover, the radiative constant (k_r) of the related transitions is around 8×10^5 s^{-1}. This value is more comparable to the one of a standard charged iridium(III) complex ([**1**][PF$_6$] and [**2**][PF$_6$] having a k_r of 3×10^5 and 4×10^5 s^{-1}, respectively),

dx.doi.org/10.1021/ic302026f | Inorg. Chem. 2013, 52, 885−897

Table 3. Photophysical Properties of the Complexes in CH_2Cl_2 (RT Liquid Solution and 77 K Rigid Matrix)

	oxygen-free solution, 298 K					77 K	
	λ_{emi} (nm)	Φ (%)	τ (ns)	k_r (10^5 s^{-1})	k_{nr} (10^8 s^{-1})	λ_{emi} (nm)	τ (μs)
[**1**][PF_6]	595	18.9	561	3.37	0.0145	520, 552	3.5
[**2**][PF_6]	535	55.2	1279	4.32	0.0035	475, 504	4.1
[**1a**][PF_6]	668	0.3	4	7.75	2.49	663, 725	~1
[**2a**][PF_6]	665	0.6	7	8.63	2.42	663, 725	~1

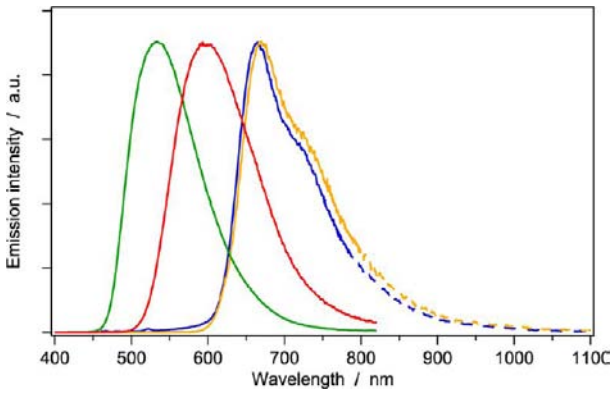

Figure 12. Normalized RT luminescence spectra, recorded in CH_2Cl_2, of the target complexes [**1a**][PF_6] (orange) and [**2a**][PF_6] (blue), compared with those of reference complexes [**1**][PF_6] (red) and [**2**][PF_6] (green); λ_{exc} = 380 nm.

rather than to the k_r of the pyr_2bpy free ligand, that is almost 500 times higher ($k_r \approx 4 \times 10^8$ s^{-1}, Table 1), or the protonated free ligand ($k_r \approx 1 \times 10^8$ s^{-1}, 125 times higher). These findings suggest that the emission of [**1a**][PF_6] and [**2a**][PF_6], though rather short-lived because of the low quantum yield, arise from the lowest triplet state of the complexes. This state is mainly centered on the pyr_2bpy ancillary ligand, as indicated by the energy and the profile of the emission band (Figure 12) and further supported by the DFT calculations (see below). The short lifetime of these triplets can be ascribed to the high spin−orbit coupling of the iridium center: this metal ion is not only acting as a positive charge (i.e., lowering the energy of the charge-transfer transition, centered on the pyr_2bpy ligand), but is also promoting the population of triplet states due to the heavy-atom effect. To further verify that these emissions arise from the complexes and not from free ligands or impurities, excitation spectra were recorded at the emission maximum (see Figure S1 in the Supporting Information) and perfectly match the corresponding absorption profile of the complex.

In Figure 13 are gathered the phosphorescence spectra in a rigid matrix at 77 K. A hypsochromic shift is observed in all cases upon going from room temperature to 77 K. As already known from literature, reference complexes [**1**][PF_6] and [**2**][PF_6] display a strong emission at 520 and 475 nm, respectively.[40] On the other hand, the corresponding pyrene-derivatives show a weak and rather structured phosphorescence around 650 nm, which resembles that of the pyr_2bpy ligand. For this reason, the 77 K emission of complexes [**1a**][PF_6] and [**2a**][PF_6] can be ascribed to a ligand-centered emission arising from the pyr_2bpy triplet, which is further red-shifted compared to the free ligand due to the presence of the positively charged

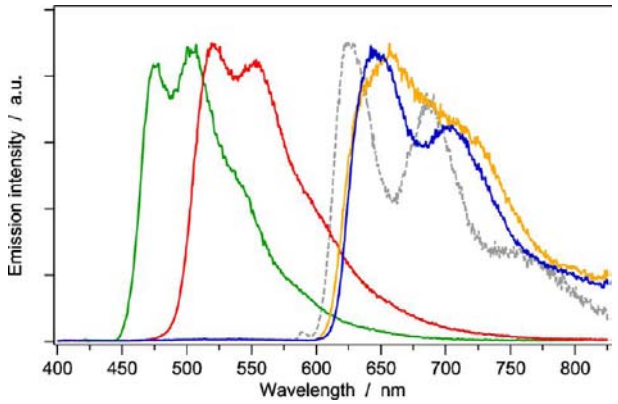

Figure 13. 77 K luminescence spectra of [**1a**][PF_6] (orange) and [**2a**][PF_6] (blue), together with reference complexes [**1**][PF_6] (red) and [**2**][PF_6] (green), all recorded in frozen CH_2Cl_2 matrix; λ_{exc} = 380 nm. The phosphorescence spectrum of the pyr_2bpy ligand is included for comparison in light gray.

iridium ion. It was impossible to obtain reliable lifetime data for the 77 K emission of [**1a**][PF_6] and [**2a**][PF_6] due to the low intensity of these emissions, the bad quality of CH_2Cl_2 frozen glass, and its occurrence in the deep-red spectral region where detectors are less sensitive. These combined circumstances make the signal-to-noise ratio extremely low.

Theoretical Description of the Ground and Excited States of Iridium(III) Complexes Based on the pyr_2bpy Ligand. In the singlet ground state (S_0), cations [**1a**]$^+$ and [**2a**]$^+$ present the typically distorted octahedral coordination geometry expected for iridium(III) complexes. Figure 14 shows

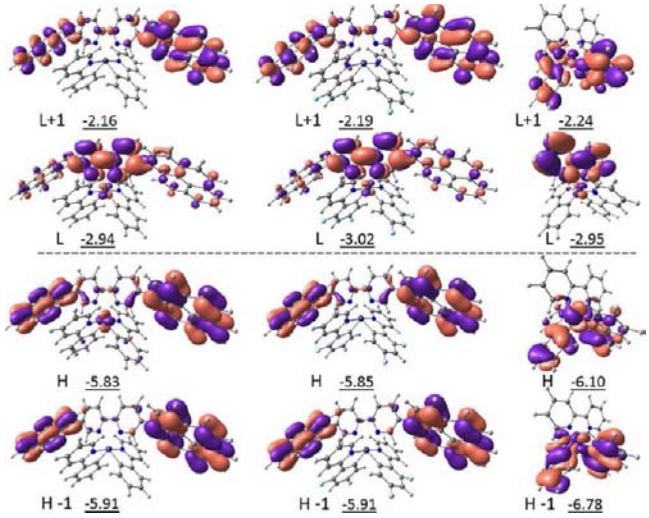

Figure 14. Electronic density contours (0.03 e $bohr^{-3}$) calculated for the HOMO, HOMO−1, LUMO and LUMO+1 (H and L denote HOMO and LUMO, respectively) of the target [**1a**]$^+$ (left) and [**2a**]$^+$ (middle) and the reference [**1**]$^+$ (right) complexes. Orbital energies are provided in eV.

the topology of the HOMOs and LUMOs calculated for the target [**1a**]$^+$ and [**2a**]$^+$ and the reference [**1**]$^+$ complexes. Compared to [**1**]$^+$ and [**2**]$^+$, for which the HOMO and HOMO−1 correspond to a mixture of Ir(III) dπ orbitals (t_{2g}) and phenyl π orbitals of the cyclometalated C^N ligands, the two highest orbitals of [**1a**]$^+$ and [**2a**]$^+$ are mainly localized on the pyrene units. In contrast, the LUMO presents the same

dx.doi.org/10.1021/ic302026f | Inorg. Chem. 2013, 52, 885−897

topology for all the complexes and mainly resides on the bpy moiety. The introduction of fluorine substituents in the cyclometalated ligands therefore has a different effect on the energies of the frontier molecular orbitals. For complex $[\mathbf{2}]^+$, it leads to a strong stabilization of the HOMO and to a smaller stabilization of the LUMO,[3a,11,39,41] and, as a consequence, the HOMO−LUMO energy gap increases and a blue-shifted absorption is observed in passing from $[\mathbf{1}]^+$ and $[\mathbf{2}]^+$ (Figure 11). The scenario is different for the pyrene-based complexes since the HOMO is located on the pyrene units and remains almost unaffected in passing from $[\mathbf{1a}]^+$ (−5.83 eV) to $[\mathbf{2a}]^+$ (−5.85 eV), whereas the LUMO is slightly stabilized (0.08 eV) owing to the direct coupling with the more positively charged $[(C\text{^}N)_2Ir]^+$ environment. As a consequence, the HOMO−LUMO gap narrows from 2.89 ($[\mathbf{1a}]^+$) to 2.83 eV ($[\mathbf{2a}]^+$) and, in line with experimental data (Figure 11), a red-shifted absorption is expected for $[\mathbf{2a}]^+$ compared to $[\mathbf{1a}]^+$. This is further corroborated by TD-DFT calculations (see below).

After establishing the major orbital effects of introducing the pyr units, the excited singlet states were investigated using the TD-DFT approach. Table 4 and Figure 15 summarize the most important singlet states that contribute to the absorption spectrum of $[\mathbf{1a}]^+$ and $[\mathbf{2a}]^+$. The excited singlet states of the reference complex $[\mathbf{1}]^+$ were also calculated for comparison purposes. There are three well-defined regions above 250 nm (Figure 15) in good agreement with the experimental spectra (Figure 11). We focus on the lowest-energy 430−500 nm region, which is mainly described by the electronic transitions to the S_2 and S_1 states for $[\mathbf{1a}]^+$ and $[\mathbf{2a}]^+$, respectively (Table 4). Both states result from the HOMO→LUMO excitation, and imply an electronic density charge transfer from the lateral pyr units to the central bpy moiety (Figure 14). The S_1 state in $[\mathbf{1a}]^+$ originates in the HOMO−2→LUMO excitation and implies a charge transfer from the Ir-ppy moiety, where the HOMO−2 is located, to the bpy unit similar to that found for the HOMO→LUMO S_1 state of $[\mathbf{1}]^+$ (Table 4 and Figure 14). The state has almost no intensity (f = 0.02−0.03) and appears at lower energies for $[\mathbf{1a}]^+$ (S_1: 2.51 eV, 494 nm) than for $[\mathbf{2a}]^+$ (S_3: 2.78 eV, 446 nm) because of the electron-withdrawing fluorine atoms attached to the ppy ligands that stabilize the HOMO−2 ($[\mathbf{1a}]^+$: −5.93 eV, $[\mathbf{2a}]^+$: −6.25 eV). Therefore, the absorption band in the 430−500 nm region is ascribed to ICT pyr→bpy transitions. TD-DFT calculations correctly predict the red-shift of the absorption maximum in passing from $[\mathbf{1a}]^+$ to $[\mathbf{2a}]^+$ (Figure 15) as the reduction of the HOMO−LUMO energy gap indicated. The absorption spectrum calculated for the reference complex $[\mathbf{1}]^+$ shows no $S_0 \rightarrow S_n$ electronic transition above 400 nm with significant intensity (Table 4 and Figure 15).

To describe the triplet excited states of $[\mathbf{1a}]^+$ and $[\mathbf{2a}]^+$, we first performed TD-DFT calculations on the ground-state fully optimized geometries (Table 4). For both complexes, the lowest-energy triplet (T_1) results from a mixing of pyr→pyr and pyr→bpy excitations and is located 1.85 and 1.83 eV above S_0 for $[\mathbf{1a}]^+$ and $[\mathbf{2a}]^+$, respectively. For the reference complex $[\mathbf{1}]^+$, T_1 is calculated at higher energies (2.59 eV) and implies a charge transfer from the Ir-ppy environment to the bpy ligand. The corresponding Ir-ppy→bpy triplets are found at similar energies for $[\mathbf{1a}]^+$ (T_4, 2.54 eV) and $[\mathbf{2a}]^+$ (T_5, 2.76 eV) (Table 4). In line with the photophysical study, TD-DFT calculations therefore indicate that emission in the target complexes $[\mathbf{1a}]^+$ and $[\mathbf{2a}]^+$ takes place from a charge transfer triplet state localized on the pyr_2bpy domain.

Table 4. TD-DFT Singlet and Triplet Excited States calculated for $[\mathbf{1a}]^+$, $[\mathbf{2a}]^+$, and $[\mathbf{1}]^+$ Complexes in CH_2Cl_2. Vertical Excitation Wavelengths (λ), Oscillator Strengths (f), Dominant Monoexcitations (with their Contribution within Parentheses), and Nature of the Electronic Transition are Provided

compd	state	λ (nm)	f^a	dominant monoexcitation	nature
$[\mathbf{1a}]^+$					
	S_1	494	0.03	H−2 → L (0.64)	Ir-ppy→bpy
	S_2	467	0.73	H → L (0.63)	pyr→bpy
	S_3	448	0.02	H−1 → L (0.70)	pyr→bpy
	S_{10}	348	0.30	H−5 → L (0.60)	pyr→bpy
	S_{11}	347	0.30	H → L+3 (0.47)	pyr→ppy
	S_{19}	335	0.21	H−1 → L+1 (0.31)	pyr→pyr
	T_1	672		H → L (0.42)	pyr→bpy
				H−1 → L+1 (0.42)	pyr→pyr
	T_2	661		H → L+1 (0.45)	pyr→pyr
				H−1 → L (0.37)	pyr→pyr
	T_3	504		H−2 → L (0.48)	Ir-ppy→bpy
				H→ L (0.34)	pyr→bpy
	T_4	487		H−2 → L (0.49)	Ir-ppy→bpy
	T_5	455		H−2 → L+2 (0.47)	Ir-ppy→ppy
$[\mathbf{2a}]^+$					
	S_1	486	0.83	H → L (0.70)	pyr→bpy
	S_2	458	0.02	H−1 → L (0.70)	pyr→bpy
	S_3	446	0.02	H−2 → L (0.69)	Ir-ppy→bpy
	S_7	356	0.39	H−3 → L (0.41)	pyr→bpy
				H → L+3(0.38)	pyr→ppy
	S_{16}	339	0.11	H−6 → L (0.52)	ppy→bpy
				H → L+1 (0.30)	pyr→pyr
	S_{17}	337	0.18	H−1→ L+1 (0.62)	pyr→pyr
	T_1	677		H → L (0.43)	pyr→bpy
				H−1 → L+1 (0.41)	pyr→pyr
	T_2	664		H → L+1 (0.44)	pyr→pyr
	T_3	500		H → L (0.43)	pyr→bpy
	T_4	456		H−1 → L (0.58)	pyr→bpy
	T_5	449		H−2→ L (0.68)	Ir-ppy→bpy
$[\mathbf{1}]^+$					
	S_1	471	0.00	H → L (0.70)	Ir-ppy→ppy
	S_2	381	0.07	H → L+1 (0.70)	Ir-ppy→ppy
	S_5	362	0.06	H−1→ L (0.61)	Ir-ppy→bpy
	S_7	344	0.05	H−2 → L (0.61)	Ir-ppy→bpy
	S_9	322	0.01	H → L+4 (0.68)	Ir-ppy→bpy
	T_1	478		H→ L (0.68)	Ir-ppy→bpy
	T_2	451		H → L+1(0.50)	Ir-ppy→ppy
	T_3	446		H → L+2(0.44)	Ir-ppy→ppy

[a]Only the singlet states with $f > 0.10$ have been included for $[\mathbf{1a}]^+$ and $[\mathbf{2a}]^+$, and those with $f > 0.01$ for $[\mathbf{1}]^+$.

To further investigate the nature of the lowest-energy triplet state, we fully optimized the geometry of T_1 by means of the UDFT approach. After full-geometry relaxation, the CT state associated to the pyr_2bpy moiety is confirmed to be the most stable triplet and is calculated to lie 1.87 ($[\mathbf{1a}]^+$) or 1.84 eV ($[\mathbf{2a}]^+$) above S_0 (adiabatic energy differences), close to the values predicted by the TD-DFT results. The nature of T_1 is confirmed by the spin-density distributions shown in Figure 16a,b, which perfectly correlate with the spin density calculated for the lowest triplet state of the pyr_2bpy ligand (Figure 10, top) and differ from that computed for $[\mathbf{1}]^+$ (Figure 16c).

Theoretical calculations therefore confirm that the lowest triplet state T_1 for the target complexes is defined as a CT

dx.doi.org/10.1021/ic302026f | Inorg. Chem. 2013, 52, 885−897

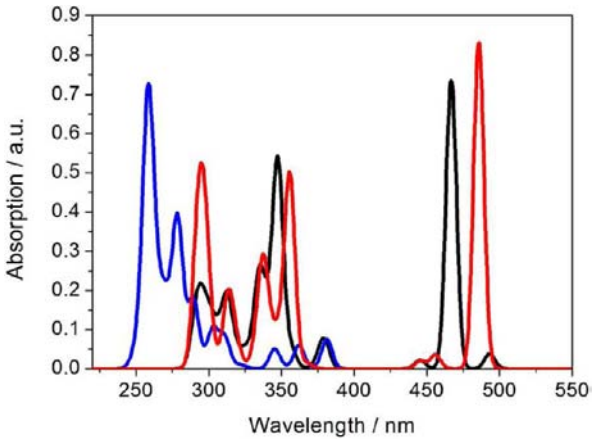

Figure 15. Calculated absorption spectra of the $[\mathbf{1a}]^+$ (black) $[\mathbf{2a}]^+$ (red) and $[\mathbf{1}]^+$ (blue) complexes in CH_2Cl_2.

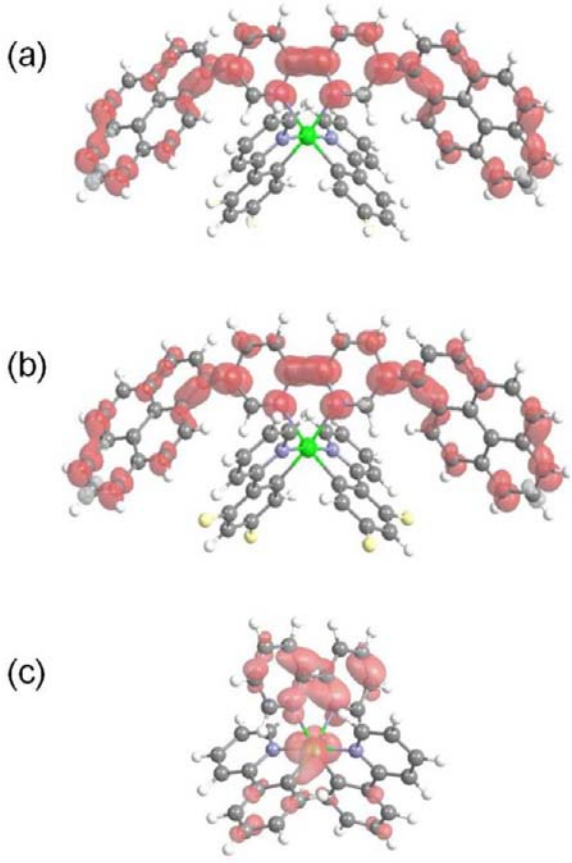

Figure 16. Spin density distributions (0.005 e bohr^{-3}) computed for the UDFT-optimized T_1 state of complexes (a) $[\mathbf{1a}]^+$, (b) $[\mathbf{2a}]^+$ and (c) $[\mathbf{1}]^+$.

^{3}pyr$_2$bpy state, and that this state is located in energy well-below the strong Ir-ppy→bpy emitting triplet states. An effective population is therefore expected for the ^{3}pyr$_2$bpy states explaining the low photoluminescence quantum yields observed for the target complexes when compared with those recorded for the reference complexes (Table 3).

CONCLUSION

The synthesis and structural X-ray characterization of two novel ionic bis-heteroleptic iridium(III) complexes incorporating a 2,2′-bipyridine ancillary ligand functionalized with pyrene groups in 5,5′-positions (pyr$_2$bpy) have been reported. A comprehensive photophysical and theoretical investigation, including comparison with model unsubstituted complexes and studies of the protonation of pyr$_2$bpy, has allowed elucidation of the role of the pyrene substituents in dictating the nature and sequence of electronic excited states, relative to those centered on the metal complex moiety. The combination of both approaches confirmed that an intramolecular charge transfer singlet state centered on the pyr$_2$bpy ligand is responsible for the intense low-energy absorption band recorded in the visible 400−500 nm range. Upon fluorination of the main cyclometalated ppy ligands, this band undergoes an unexpected red-shift because of the location on the pyrene units of the HOMO level, which remains mostly unaffected, and to the electrostatic stabilization of the LUMO. Regarding the emission properties, both the photophysical and the theoretical studies establish that the lowest triplet state (T_1) of the new complexes corresponds to the lowest triplet of the pyr$_2$bpy ligand that is located lower in energy than the strong MLCT emitting states centered on the iTMC. The population of the ^{3}pyr$_2$bpy levels explains the low photoluminescence quantum yield observed for the target complexes. Noteworthy and in contrast to what has been observed for neutral iridium(III) complexes bearing aromatic substituents, the phosphorescence of the ^{3}pyr$_2$bpy state has been successfully recorded both at room and low temperature conditions. These results demonstrate that, by suitable chemical design and excited state engineering,[42] it is possible to make multi-chromophoric Ir(III) complexes whose luminescence properties are not centered on the Ir-based moiety, but where the metal center is nonetheless active in dictating the luminescence output by electrostatic interactions. This result further widens the scope of Ir complexes as versatile and tunable luminescent materials, taking advantage of thoroughly chosen chromophoric/luminophoric appendages on the ancillary noncyclometallating ligand.

ASSOCIATED CONTENT

Supporting Information

Excitation spectrum of $[\mathbf{1a}][PF_6]$ in CH_2Cl_2, together with absorption and emission profiles. Theoretical study on $[\mathbf{1}]^+$ using different functionals; comparison of ground-state optimized geometries and simulated absorption spectra. This material is available free of charge via the Internet at http://pubs.acs.org.

AUTHOR INFORMATION

Corresponding Author

*E-mail: catherine.housecroft@unibas.ch (C.H.); nicola.armaroli@cnr.it (N.A.); enrique.orti@uv.es (E.O.).

Present Address

#Friedrich-Alexander-Universität Erlangen-Nürnberg, Department of Chemistry and Pharmacy & Interdisciplinary Center for Molecular Materials (ICMM), Egerlandstrasse 3, D-91058, Erlangen, Germany

Notes

The authors declare no competing financial interest.

ACKNOWLEDGMENTS

We acknowledge the financial support of the European Union (CELLO, STRP 248043), the European Research Council

(Advanced Grant 267816 LiLo), the Swiss National Science Foundation, the University of Basel, the CNR (Commessa PM.P04.010, MACOL), the Spanish Ministry of Economy and Competitiveness (MINECO) (CTQ2009-08790 and Consolider-Ingenio CSD2007-00010), and the Generalitat Valenciana (PROMETEO/2012/053). We thank Jonas Schönle and Cathrin Ertl for recording 600 and 500 MHz NMR spectra. We thank Rubén Casillas (Friedrich-Alexander-Universität Erlangen-Nürnberg) for assistance with calculations and R.D.C. acknowledges the Humboldt Foundation for its support.

REFERENCES

(1) (a) Baldo, M. A.; O'Brien, D. F.; You, Y.; Shoustikov, A.; Sibley, S.; Thompson, M. E.; Forrest, S. R. *Nature* **1998**, *395*, 151. (b) Chou, P. T.; Chi, Y. *Chem.—Eur. J.* **2007**, *13*, 380. (c) Costa, R. D.; Ortí, E.; Bolink, H. J.; Graber, S.; Housecroft, C. E.; Constable, E. C. *Adv. Funct. Mater.* **2010**, *20*, 1511. (d) Costa, R. D.; Ortí, E.; Bolink, H. J.; Graber, S.; Housecroft, C. E.; Constable, E. C. *J. Am. Chem. Soc.* **2010**, *132*, 5978. (e) Costa, R. D.; Ortí, E.; Bolink, H. J.; Graber, S.; Schaffner, S.; Neuburger, M.; Housecroft, C. E.; Constable, E. C. *Adv. Funct. Mater.* **2009**, *19*, 3456. (f) Handy, E. S.; Pal, A. J.; Rubner, M. F. *J. Am. Chem. Soc.* **1999**, *121*, 3525. (g) He, L.; Duan, L.; Qiao, J.; Dong, G.; Wang, L.; Qi, Y. *Chem. Mater.* **2010**, *22*, 3535. (h) He, L.; Qiao, J.; Duan, L.; Dong, G.; Zhang, D.; Wang, L.; Qiu, Y. *Adv. Funct. Mater.* **2009**, *19*, 2950. (i) Kafafi, Z. H., *Organic Electroluminescence*. CRC Press, Boca Raton, FL: 2005. (j) Reineke, S.; Lindner, F.; Schwartz, G.; Seidler, N.; Walzer, K.; Lüssem, B.; Leo, K. *Nature* **2009**, *459*, 234. (k) Slinker, J.; Bernards, D.; Houston, P. L.; Abruña, H. D.; Bernhard, S.; Malliaras, G. G. *Chem. Commun.* **2003**, 2392. (l) Slinker, J. D.; Rivnay, J.; Moskowitz, J. S.; Parker, J. B.; Bernhard, S.; Abruña, H. D.; Malliaras, G. G. *J. Mater. Chem.* **2007**, *17*, 2976. (m) Ulbricht, C.; Beyer, B.; Friebe, C.; Winter, A.; Schubert, U. S. *Adv. Mater.* **2009**, *21*, 4418. (n) Wu, A. P.; Lee, J. K.; Rubner, M. F. *Thin Solid Films* **1998**, *329*, 663. (o) Wu, A. P.; Yoo, D. S.; Lee, J. K.; Rubner, M. F. *J. Am. Chem. Soc.* **1999**, *121*, 4883. (p) Yan, B.; Cheung, C. C. C.; Kui, S. C. F.; Xiang, H.; Roy, V. A. L.; Xu, S.; Che, C. *Adv. Mater.* **2007**, *19*, 3599. (q) Yersin, Y., *Highly Efficient OLEDs with Phosphorescent Materials*; Wiley-VCH: Weinheim, Germany, 2007.

(2) (a) Wang, P.; Zakeeruddin, S. M.; Moser, J. E.; Nazeeruddin, M. K.; Sekiguchi, T.; Grätzel, M. *Nat. Mater.* **2003**, *2*, 402. (b) Grätzel, M. *Nature* **2001**, *414*, 338. (c) Lu, X.; Wang, F.; Li, Y. *ACS Appl. Mater. Interfaces* **2010**, *2*, 1980. (d) Hardin, B. E.; Yum, J.-H.; Hoke, E. T.; Jun, Y. C.; Péchy, P.; Torres, T.; Brongersma, M. L.; Nazeeruddin, M. K.; Grätzel, M.; McGehee, M. D. *Nano Lett.* **2010**, *10*, 3077. (e) Chiba, Y.; Islam, A.; Watanabe, Y.; Komiya, R.; Koide, N.; Han, L. *Jpn. J. Appl. Phys.* **2006**, *45*, L638. (f) Nazeeruddin, M. K.; Liska, P.; Moser, J. E.; Vlachopoulos, N.; Grätzel, M. *Helv. Chim. Acta* **1990**, *73*, 1788. (g) O'Reagan, B.; Gratzel, M. *Nature* **1991**, *353*, 737. (h) Bach, U.; Lupo, D.; Comte, P.; Moser, J. E.; Weissörtel, F.; Salbeck, J.; Spreitzer, H.; Grätzel, M. *Nature* **1998**, *395*, 583. (i) Kim, J.-J.; Lim, K.; Choi, H.; Fan, S.; Kang, M.-S.; Gao, G.; Kang, H. S.; Ko, J. *Inorg. Chem.* **2010**, *49*, 8351.

(3) (a) Costa, R. D.; Ortí, E.; Bolink, H.; Monti, F.; Accorsi, G.; Armaroli, N. *Angew. Chem., Int. Ed. Engl.* **2012**, *51*, 8178. (b) Hu, T.; He, L.; Duan, L.; Qiu, Y. *J. Mater. Chem.* **2012**, *22*, 4206.

(4) Brandel, J.; Sairenji, M.; Ichikawa, K.; Nabeshima, T. *Chem. Commun.* **2010**, *46*, 3958.

(5) See for example: Lowry, M. S.; Goldsmith, J. I.; Slinker, J. D.; Rohl, R.; Pascal, R. A.; Malliaras, G. G.; Bernhard, S. *Chem. Mater.* **2005**, *17*, 5712.

(6) (a) Edkins, R. M.; Bettington, S. L.; Goeta, A. E.; Beeby, A. *Dalton Trans* **2011**, *40*, 12765. (b) Girardot, C.; Cao, B.; Mulatier, J.-C.; Baldeck, P. L.; Chauvin, J.; Riehl, D.; Delaire, J. A.; Andraud, C.; Lemercier, G. *ChemPhysChem* **2008**, *9*, 1531. (c) Natrajan, L. S.; Toulmin, A.; Chewa, A.; Magennis, S. W. *Dalton Trans.* **2010**, *39*, 10837. (d) Four, M.; Riehl, D.; Mongin, O.; Blanchard-Desce, M.; Lawson-Daku, L. M.; Moreau, J.; Chauvin, J.; Delairef, J. A.; Lemercier, G. *Phys. Chem. Chem. Phys.* **2011**, *13*, 17304. (e) Samoc, M.; Morrall, J. P.; Dalton, G. T.; Cifuentes, M. P.; Humphrey, M. G. *Angew. Chem., Int. Ed.* **2007**, *46*, 731. (f) Morrall, J. P.; Dalton, G. T.; Humphrey, M. G.; Samoc, M. Organotransition Metal Complexes for Nonlinear Optics. In *Advances in Organometallic Chemistry*; Elsevier: Amsterdam, 2007; Vol. *55*, 61−136. (g) Girardot, C.; Lemercier, G.; Mulatier, J.-C.; Chauvin, J.; Baldeck, P. L.; Andraud, C. *Dalton Trans.* **2007**, 3421.

(7) (a) Schwartz, K. R.; Chitta, R.; Bohnsack, J. N.; Ceckanowicz, D. J.; Miró, P.; Cramer, C. J.; Mann, K. R. *Inorg. Chem.* **2012**, *51*, 5082. (b) Costa, R. D.; Céspedes-Guirao, F. J.; Ortí, E.; Bolink, H. J.; Gierschner, J.; Fernández-Lázaro, F.; Sastre-Santos, A. *Chem. Commun.* **2009**, 3886. (c) Rachford, A. A.; Ziessel, R.; Bura, T.; Retailleau, P.; Castellano, F. N. *Inorg. Chem.* **2010**, *49*, 3730.

(8) (a) Geddes, C. D.; Lakowicz, J. R. *Advanced Concepts in Fluorescence Spectroscopy: Macromolecular Sensing*; Springer: New York, 2005. (b) Yamana, K.; Takei, M.; Nakano, H. *Tetrahedron Lett.* **1997**, *38*, 6051. (c) Hariharan, M.; Karunakaran, S. C.; Ramaiah, D. *Org. Lett.* **2007**, *9*, 417. (d) Choi, J. K.; Kim, S. H.; Yoon, S. J.; Lee, K.-H.; Bartsch, R. A.; Kim, J. S. *J. Org. Chem.* **2006**, *71*, 8011. (e) Xiang, J.; Zhu, D. *Org. Lett.* **2008**, *10*, 2271. (f) Ding, S.-N.; Shan, D.; Cosnier, S.; Le Goff, A. *Chem.— Eur. J.* **2012**, DOI: 10.1002/chem.201201543.

(9) Spaenig, F.; Olivier, J.-H.; Prusakova, V.; Retailleau, P.; Ziessel, R.; Castellano, F. N. *Inorg. Chem.* **2011**, *50*, 10859.

(10) Sprouse, S.; King, K. A.; Spellane, P. J.; Watts, R. J. *J. Am. Chem. Soc.* **1984**, *106*, 6647.

(11) Lafolet, F.; Welter, S.; Popović, Z.; De Cola, L. *J. Mater. Chem.* **2005**, *15*, 2820.

(12) Romero, F. M.; Ziessel, R. *Tetrahedron Lett.* **1995**, *36*, 6471.

(13) Henze, O.; Lehmann, U.; Schlüter, A. D. *Synthesis* **1999**, 683.

(14) Schwab, P. F. H.; Fleischer, F.; Michl, J. *J. Org. Chem.* **2002**, *67*, 443.

(15) *IPDS software* v 1.26; Stoe & Cie: Darmstadt, Germany, 1996.

(16) Sheldrick, G. M. *Acta Crystallogr., Sect. A* **2008**, *64*, 112.

(17) *COLLECT Software*; Nonius BV: , 1997−2001.

(18) Otwinowski, Z.; Minor, W., *Methods in Enzymology*;Carter, C.W., Jr., Sweet, R.M., Eds.; Academic Press: New York, 1997; Vol. *276*, pp 307.

(19) Altomare, A.; Cascarano, G.; Giacovazzo, G.; Guagliardi, A.; Burla, M. C.; Polidori, G.; Camalli, M. *J. Appl. Crystallogr.* **1994**, *27*, 435.

(20) Betteridge, P. W.; Carruthers, J. R.; Cooper, R. I.; Prout, K.; Watkin, D. J. *J. Appl. Crystallogr.* **2003**, *36*, 1487.

(21) Farrugia, L. J. *J. Appl. Crystallogr.* **1997**, *30*, 565.

(22) Bruno, I. J.; Cole, J. C.; Edgington, P. R.; Kessler, M. K.; Macrae, C. F.; McCabe, P.; Pearson, J.; Taylor, R. *Acta Crystallogr., Sect. B* **2002**, *58*, 389.

(23) Macrae, C. F.; Bruno, I. J.; Chisholm, J. A.; Edgington, P. R.; McCabe, P.; Pidcock, E.; Rodriguez-Monge, L.; Taylor, R.; van de Streek, J.; Wood, P. A. *J. Appl. Crystallogr.* **2008**, *41*, 466.

(24) Demas, J. N.; Crosby, G. A. *J. Phys. Chem.* **1971**, *75*, 991.

(25) Nakamaru, K. *Bull. Chem. Soc. Jpn.* **1982**, *55*, 2697.

(26) Frisch, M. J.; Trucks, G. W.; Schlegel, H. B.; Scuseria, G. E.; Robb, M. A.; Cheeseman, J. R.; Scalmani, G.; Barone, V.; Mennucci, B.; Petersson, G. A.; Nakatsuji, H.; Caricato, M.; Li, X.; Hratchian, H. P.; Izmaylov, A. F.; Bloino, J.; Zheng, G.; Sonnenberg, J. L.; Hada, M.; Ehara, M.; Toyota, K.; Fukuda, R.; Hasegawa, J.; Ishida, M.; Nakajima, T.; Honda, Y.; Kitao, O.; Nakai, H.; Vreven, T.; Montgomery, J., J., A.; ; Peralta, J. E.; Ogliaro, F.; Bearpark, M.; Heyd, J. J.; Brothers, E.; Kudin, K. N.; Staroverov, V. N.; Kobayashi, R.; Normand, J.; Raghavachari, K.; Rendell, A.; Burant, J. C.; Iyengar, S. S.; Tomasi, J.; Cossi, M.; Rega, N.; Millam, N. J.; Klene, M.; Knox, J. E.; Cross, J. B.; Bakken, V.; Adamo, C.; Jaramillo, J.; Gomperts, R.; Stratmann, R. E.; Yazyev, O.; Austin, A. J.; Cammi, R.; Pomelli, C.; Ochterski, J. W.; Martin, R. L.; Morokuma, K.; Zakrzewski, V. G.; Voth, G. A.; Salvador, P.; Dannenberg, J. J.; Dapprich, S.; Daniels, A. D.; Farkas, Ö.; Foresman, J. B.; Ortiz, J. V.; Cioslowski, J.; Fox, D. J. *Gaussian 09; Revision A.1*; Gaussian, Inc.:Wallingford, CT, 2009.

(27) (a) Becke, A. D. *J. Chem. Phys.* **1988**, *88*, 2547. (b) Becke, A. D. *Phys. Rev. A* **1988**, *38*, 3098. (c) Becke, A. D. *J. Chem. Phys.* **1993**, *98*, 5648.

(28) (a) Becke, A. D. *J. Chem. Phys.* **1996**, *104*, 1040. (b) Burke, K.; Perdew, J. P.; Wang, Y. In *Electronic Density Functional Theory: Recent Progress and New Directions*; Dobson, J. F., Vignale, G., Das, M. P., Eds.; Plenum: New York, 1998. (c) Lee, C.; Yang, W.; Parr, R. G. *Phys. Rev. B* **1998**, *37*, 785. (d) Perdew, J. P. In *Electronic Structure of Solids '91*; Ziesche, P., Eschrig, H., Eds.; Akademie Verlag: Berlin, 1991; p 11.
(29) Adamo, C.; Barone, V. *J. Chem. Phys.* **1998**, *108*, 664.
(30) (a) Henderson, T. M.; Izmaylov, A. F.; Scalmani, G.; Scuseria, G. E. *J. Chem. Phys.* **2009**, *131*, 044108. (b) Ernzerhof, M.; Perdew, J. P. *J. Chem. Phys.* **1998**, *109*, 3313.
(31) Zhao, Y.; Truhlar, D. G. *Theor. Chem. Acc.* **2008**, *120*, 215.
(32) Francl, M. M.; Pietro, W. J.; Hehre, W. J.; Binkley, J. S.; Gordon, M. S.; Defrees, D. J.; Pople, J. A. *J. Chem. Phys.* **1982**, *77*, 3654.
(33) Hay, P. J.; Wadt, W. R. *J. Chem. Phys.* **1985**, *82*, 299.
(34) (a) Cramer, C. S.; Truhlar, D. G., *Solvent Effects and Chemical Reactivity*; Kluwer: Dordrecht, The Netherlands, 1996. (b) Tomasi, J.; Persico, M. *Chem. Rev.* **1994**, *94*, 2027.
(35) Janiak, C. *J. Chem. Soc., Dalton Trans.* **2000**, 3885.
(36) Robertson, J. M.; White, J. G. *J. Chem. Soc.* **1947**, 358.
(37) Harriman, A.; Hissler, M. *Phys. Chem. Chem. Phys.* **1999**, *1*, 4203.
(38) Nakamoto, K. *J. Phys. Chem.* **1960**, *64*, 1420. Moissette, A.; Batonneau, Y.; Brémard, C. *J. Am. Chem. Soc.* **2001**, *123*, 12325.
(39) Bolink, H. J.; Coronado, E.; Costa, R. D.; Lardiés, N.; Ortí, E. *Inorg. Chem.* **2008**, *47*, 9149.
(40) Costa, R. D.; Monti, F.; Accorsi, G.; Barbieri, A.; Bolink, H. J.; Ortí, E.; Armaroli, N. *Inorg. Chem.* **2011**, *50*, 7229.
(41) Lowry, M. S.; Hudson, W. R.; Pascal, R. A.; Bernhard, S. *J. Am. Chem. Soc.* **2004**, *126*, 14129.
(42) Armaroli, N. *ChemPhysChem* **2008**, *9*, 371.